Journal of Materials Chemistry C

ROYAL SOCIETY OF CHEMISTRY

PAPER

View Article Online
View Journal | View Issue

Cite this: J. Mater. Chem. C, 2022, 10, 14306

Dithia[9]helicenes: Molecular design, surface imaging, and circularly polarized luminescence with enhanced dissymmetry factors†

Bianca C. Baciu,[a] Pawel J. Bronk,[a] Tamara de Ara,[b] Rafael Rodriguez,[c] Pierpaolo Morgante,[e] Nicolas Vanthuyne,[d] Carlos Sabater,[b] Carlos Untiedt,[b] Jochen Autschbach,*[e] Jeanne Crassous*[c] and Albert Guijarro*[a]

Received 11th July 2022,
Accepted 3rd September 2022

DOI: 10.1039/d2tc02910c

rsc.li/materials-c

Synthesis of two dithia[9]helicenes by means of a LED-based double photocyclization is reported. The compounds have sulfur atoms placed at the terminal rings of the helicene, and they display two alternative C_2-symmetrical arrangements named *exo* (**1**) and *endo* (**2**). Separation of enantiomers of opposite helicity allowed the complete characterization in solution, *in silico*, by X-ray crystallography, and adsorbed on gold. The theoretical analysis confirms the unexpected finding that *endo*-dithia[9]helicene displays an experimental dissymmetry factor (g_{lum}) in CPL larger than its isomer *exo*-dithia[9]helicene (−0.0125 *vs.* −0.0042). This enhanced g_{lum} factor ranks among the largest for a helicene-type molecule. Comparison with smaller analogues, namely *exo* and *endo*-dithia[7]helicenes (**10** and **11**, respectively), is also presented.

Introduction

Helicenes display a robust, fully conjugated helical architecture that makes them prototypes of chiral polyaromatic hydrocarbons with an ever-increasing range of applications.[1] For example, much attention has been focused on circularly polarized luminescence (CPL) for future potential applications in cryptography, circularly polarized organic light-emitting diode (OLED) technology, bioimaging, or photocatalysis.[2] A chiral excited molecule imprints its chirality on the emitted photon, thus causing the emission to acquire right-handed or left-handed circular polarization (RCP, LCP).[3] The efficiency of CPL is quantified by the emission dissymmetry factor, $g_{lum} = 2(I_L - I_R)/(I_L + I_R)$, where I_L and I_R refer to LCP and RCP of the luminescence intensity. The dissymmetry factor is typically in the 10^{-3} to 10^{-5} range for small organic molecules.[4] For transitions that are not electric dipole-forbidden, and in the Gaussian units commonly used for optical activity, $g_{lum} = 4Im[\vec{\mu}_e \cdot \vec{\mu}_m^*]/|\mu_e|^2$. Subscripts *e* and *m* refer to the ground-to-excited state electric and magnetic transition dipole moment (TDM), respectively, and *Im* indicates the imaginary part of the scalar product of these vectors. In the case of electric dipole-forbidden transitions, terms of higher order in the multipole expansion of the electromagnetic wave would need to be considered, but they can be neglected for the present work. For g_{lum} to be nonzero, the electric and magnetic TDM must not be perpendicular or individually vanish, a condition only fulfilled for chiral molecules.[3] Thus, $g_{lum} = 4\cos\theta|\mu_m^*|/|\mu_e|$, with θ representing the angle between the transition moments.[5,6] Endowed with an inherently chiral chromophore, the application of simple carbohelicenes as CPL emitters has been the focus of intense research in the last decade.[7] Compared to fully carbonated systems, the synthesis of heterohelicenes aims not only to create new structures but also to adjust their photophysical properties,[8] providing new helicene-related emitters with improved properties.[9,10] Among them, the best performing compounds typically exhibit a g_{lum} in the range 10^{-2}–10^{-3}.[11]

Thiahelicenes represent an important class of heterohelicenes because they combine both high electronic properties arising from polythiophene materials along with intriguing chiroptical properties that can be reached when dealing with helical chirality.[12] Thiahelicenes have significant advantages with respect to simpler carbohelicenes, that include (i) the

[a] Departamento de Química Orgánica and Instituto Universitario de Síntesis Orgánica, Unidad asociada CSIC, Universidad de Alicante, Campus de San Vicente del Raspeig, E-03080, Alicante, Spain. E-mail: aguijarro@ua.es
[b] Departamento de Fisica Aplicada and Unidad asociada CSIC, Universidad de Alicante, Campus de San Vicente del Raspeig, E-03080, Alicante, Spain
[c] Université Rennes, CNRS, ISCR-UMR 6226, Rennes, F-35000, France. E-mail: jeanne.crassous@univ-rennes1.fr
[d] Aix Marseille University, CNRS, Centrale Marseille, iSm2, Marseille, France
[e] Department of Chemistry, University at Buffalo, State University of New York, Buffalo, New York, 14260, USA. E-mail: jochena@buffalo.edu

† Electronic supplementary information (ESI) available. CCDC 2184340 and 2184341. For ESI and crystallographic data in CIF or other electronic format see DOI: https://doi.org/10.1039/d2tc02910c

lower oxidation potentials which present an essential parameter for application as conducting organic materials; (ii) the easier functionalization of the thiahelicene backbone, either in the α position or in the β position of the terminal thiophene rings; (iii) a plethora of short intermolecular S–S (and of S to other atoms) contacts along with the π–π stackings in the solid state. All these features offer new opportunities to design novel organic semiconductors with high carrier mobility and original (chir)optical properties. Among the different classes of thiahelicenes, readily accessible tetrathiahelicenes have monopolized much of the attention.[13] We have recently reported a synthetic procedure to access dithiahelicenes with the sulfur atoms located in the first and last rings, but pointing inwards to the helical axis in what was called the *endo*-isomer, namely in the form of *endo*-dithia[7]helicene, in addition to the more easily accessible *exo*-isomer with the sulfur atom pointing outwards.[14] In this work we propose the preparation of *exo*-dithia[9]helicene **1** and *endo*-dithia[9]helicene **2**, presented in Scheme 2. We performed a detailed characterization in solution, in the solid state and on a gold surface, and analyzed the chiroptical properties of these new compounds. We found strong CPL activity, with emission dissymmetry factors as high as 1.2×10^{-2}. The paper is organized as follows: (a) synthesis of these molecules using a LED photocyclization as a key step; (b) characterization in the solid state by X-ray crystallography; (c) experimental photophysical and chiroptical properties of *exo*-**1** and *endo*-**2**, as well as of their smaller [7]homologues; (d) simulated spectra and theoretical analysis, and (e) characterization on a gold surface by scanning tunneling microscopy (STM).

Results and discussion

Synthesis of *exo*-dithia[9]helicene-1 and *endo*-dithia[9]helicene-2

Based on our previous experience with the preparation of *exo*- and *endo*-dithia[7]helicenes in good yields,[14,15] we propose now the synthesis of *exo*- and *endo*-dithia[9]helicenes **1** and **2**. The synthetic pathways used for this modular synthesis adapted our state of the art methods of Pd-catalyzed coupling reactions with a key final double photocyclization step of a symmetric bis-stilbenic precursor, yielding the desired thiahelicene regiochemistry.

These bis-stilbenic precursor compounds were prepared following the general synthetic route depicted in Scheme 1. Starting from commercial 5- and 6-bromobenzo[*b*]thiophene (**A** and **B**, respectively), the compounds **3** and **4** were synthesized by means of a Sonogashira reaction using tri(methylsilyl)acetylene followed by the desilylation in basic medium. Then with the hydroboration of **3** and **4** we obtain the vinylboronic derivatives needed for the subsequent Suzuki coupling with the central fragment of the ensemble **7**. This fragment, 3,6-dibromophenanthrene (**7**), was easily prepared from commercially available starting materials.[14] The hydroboration was done by means of bis(pinacolatodiboron) (B_2Pin_2) through a copper catalyzed reaction activated by bidentate diphosphine ligand, Xantphos, which afforded the I-vinylboronate **5** and **6** in good yield. Bis-stilbenic precursors **8** and **9** were obtained by a Suzuki coupling of **5** and **6** with the central symmetric fragment **7** in good yields. These precursors were ready for the key photocyclization step. One of the strengths of this step is the high regioselectivity displayed by the process. It is worth

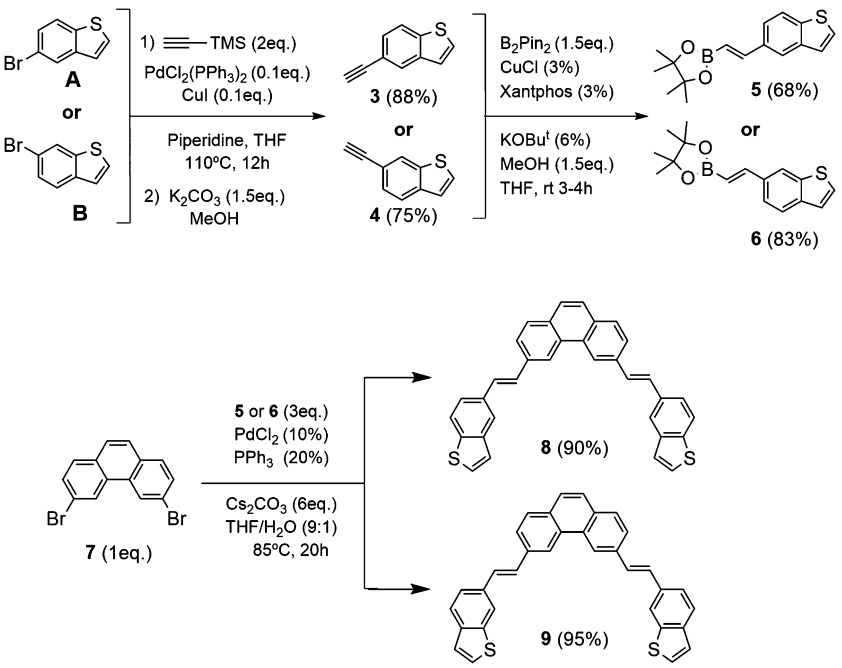

Scheme 1 Synthesis of 3,6-bis-((*E*)-2-(benzo[*b*]thiophen-5-yl)vinyl)phenanthrene (**8**) and 3,6-bis-((*E*)-2-(benzo[*b*]thiophen-6-yl)vinyl)phenanthrene (**9**).

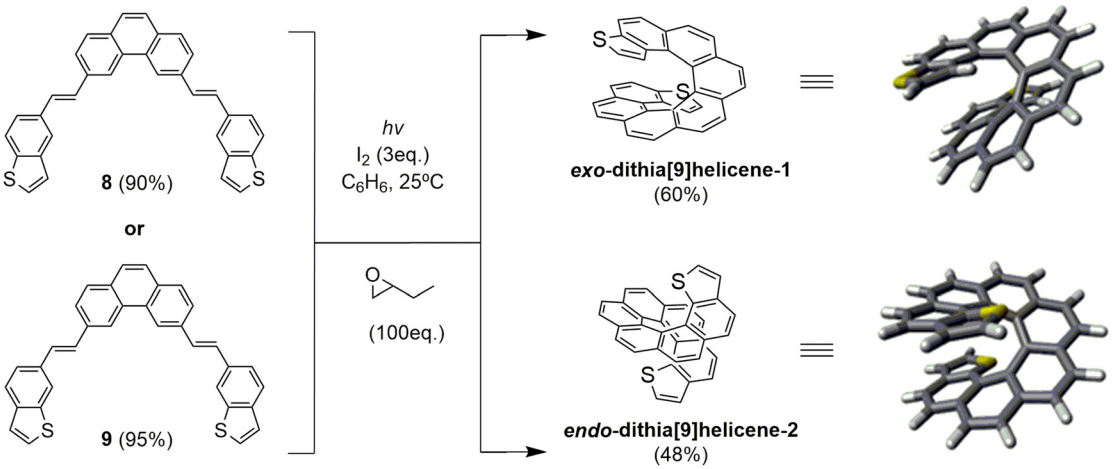

Scheme 2 Photochemical synthesis of racemic dithia[9]helicenes **1** and **2** *via* double photocyclization of bis-stilbenic precursors **8** and **9**.

recalling at this point that there are two stilbenic moieties, one on each side of the molecule, undergoing a sequential double photocyclization. Each side could in principle photocyclize in 4 different fashions. This leaves, after omitting equivalent compounds, a total of 10 possible regioisomers as final products (all the possible structures of the isomers for the *exo* and *endo* series are illustrated in the ESI,† Fig. S1). Among them, the desired helicene final product, *i.e.* with fully *ortho*-fused rings was the only successfully detected, isolated and characterized.

Bis-stilbenic compounds **8** and **9** were initially subjected to irradiation using a 400 W high-pressure Hg lamp to undergo a sequential double photocyclization under typical Mallory-Katz conditions.[16] Irradiation was carried out in benzene under refluxing conditions (3–4 hours). In both cases the final products were obtained (52% and 38% yield for **1** and **2** by 300 MHz ^{1}H-NMR analysis), contaminated with unidentified byproducts of polymeric nature that made the purification step tedious.

Our objective at this point was to improve the photochemical setup by introducing UV LED technology in the light of our previous studies on the UV-vis absorption spectra of related bis-stilbenic compounds.[14] We built a new cylindrical aluminum minireactor which incorporated two 50 W air-refrigerated LED chip sources emitting at 365 nm on opposite sides of the cylinder walls. The top of the reaction tube was connected to a silicone bubbler, placed in the center of the reactor cylinder standing up vertical and was magnetically stirred from the bottom during irradiation. After optimizing the conditions of the new system, we obtained a much cleaner ^{1}H-NMR spectrum than in the case of the high-pressure vapor Hg lamp. The sample was conveniently irradiated overnight. Not only the reaction yields were slightly improved (60% and 48% isolated yield for **1** and **2**, respectively), but the safety of the system was noticeably improved since irradiation was carried out at ambient conditions, avoiding intense refluxing of benzene due to heat overproduction as in the previous case.

The reaction afforded the expected racemic *exo*-dithia[9]-helicene-**1** from **8** and *endo*-dithia[9]helicene-**2** from **9**, which were easily purified and fully characterized (see ESI†). A distinctive fingerprint useful in the structural elucidation of this type of thiahelicene by ^{1}H-NMR are the two doublets originated by the coupling of the vicinal hydrogens of the thiophene ring. They can be distinguished in the spectrum for two reasons: (a) within the framework of a helicenic structure, the thiophene hydrogens are shifted upfield because of the anisotropic effect of the rest of the underlying aromatic structure; (b) the coupling constant (J) of these vicinal hydrogens is smaller than the other aromatic constants. The result is a pair of easily identifiable doublets in the 6–7 ppm region with J around 5–6 Hz. In the case of **1** there are two doublets at 6.50 (dd, J = 5.5 0.4 Hz, 2H) and 6.00 (dd, J = 5.5 0.8 Hz, 2H), and in the case of **2**, these two doublets are at 6.88 (d, J = 5.4 Hz, 2H) and 6.72 (d, J = 5.4 Hz, 2H).

HPLC separations over chiral stationary phases enabled to obtain enantiomeric samples (ee > 99.5%) of **1** and **2**. For the sake of comparison, smaller analogues, *i.e.* previously reported racemic *exo* and *endo*-dithia[7]helicene **10** and **11**, were separated into pure enantiomers by the same method (ee > 99.5%, see ESI† for details).

Crystal structures of *exo* and *endo*-dithia[9]helicenes 1 and 2

The compounds crystallized in small, somewhat weakly diffracting crystals that nonetheless allowed for resolute molecular/isomeric characterization, corroborating beyond doubt the isomeric molecular structure that arises from the synthesis. Diffraction data acquisition was performed at room temperature. Space group assignment was carried out under these conditions. Dynamic disorder and weak diffraction in one of the crystal dimensions were some issues that had to be overcome in the packing characterization. Nevertheless, fruitful information about solid state organization can be obtained. In the solid state, *exo*-**1** and *endo*-**2** display a monoclinic, quasi-orthorhombic unit cell with quite different type of packing, both among themselves and also when compared to their shorter [7]homologues.[15] The crystal structure of *exo*-**1** is quite intricate. It has two non-symmetrically equivalent molecular

units (type A and B) in a very large unit cell containing 16 molecules overall. A homochiral columnar arrangement of molecules ABAB in the *a* direction (longest axis) is a characteristic feature of this structure. The cell density of *exo*-**1** is 1.418 g cm^{-3}. A much simpler unit cell is found in *endo*-**2**, with only one symmetrically independent molecule and overall 4 molecules per cell. The density of this cell is 1.382 g cm^{-3}, appreciably lower than its *exo* isomer. The difference between the two cells is likely due to the larger van der Waals radius of the sulfur atom compared to carbon, which results in a slightly longer helical axis and an increased volume of the *endo* compound. Despite these differences, both unit cells are centrosymmetric, and they include an equal number of molecules displaying *P* and *M* helicities that are located opposite to each other with respect to the inversion center of the unit cell. There are no crystal structures reported for carbo[9]helicene derivatives, so a structural comparison with carbohelicene was not possible. The geometries of the individual dithiahelicenes, although slightly distorted form the ideal C_2 symmetry due to the crystal packing, match very well the theoretically calculated structures, as shown visually and numerically in Fig. 1 for both compounds. The root mean squared deviations (RMSDs) reported in Fig. 1 were calculated considering only heavy atoms,[17] and they indicate geometrical deviations in the typical range of most functional/small basis set combinations.[18] The dihedral angles (φ) of the edge of the inner helix, starting from C_1 in **1** or S_1 in **2**, were used as a geometrical parameter to compare the helicene structures.[19] The experimental values from the X-ray structures followed by the standard uncertainty (in parentheses) are 11(1), 28(1), 26(1), 22(1), 28(1), 23(1), and 11(1)° for the type A molecule of *exo*-**1**, and 10(1), 26(1), 28(1), 17(1), 30(1), 23(1), and 8(1)° for the type B molecule. The angles add up 149° (A) and 142° (B), respectively, with standard uncertainties of ±3°, revealing a relatively compressed B type of coil respect to A in the solid. For the *endo* isomer, the angles are 10(1), 23(1), 31(1), 18(1), 28(1), 30(1), and 9(1)°, adding up to 149° also with ±3° of standard uncertainty. This shows a slightly stretched *endo* isomer coil in comparison to the average *exo* isomer.

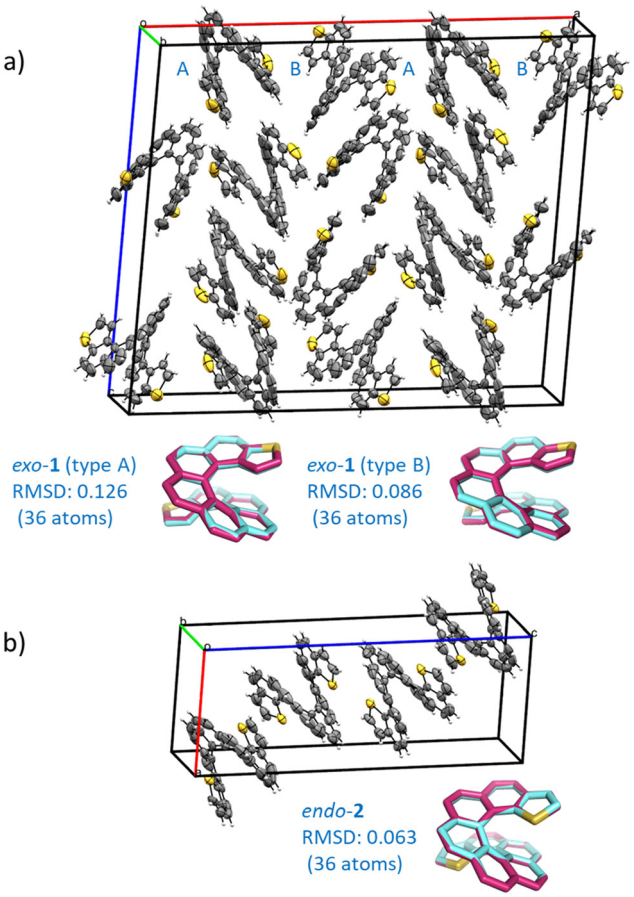

Fig. 1 (a) Crystal structure of the racemate *exo*-dithia[9]helicene (**1**): Monoclinic unit cell, space group *C*2/*c*, *a* = 33.075(4), *b* = 9.8984(11), *c* = 28.178(3) (Å); α = 90, β = 94.890(2), γ = 90°; *Z* = 16; CCDC number 2184340. The experimental structures of both molecular types found in the unit cell (A and B, reported in cyan) are overlapped with the calculated CAM-B3LYP/def2-SV(P) structures (in magenta) and shown below the unit cell; (b) crystal structure of the racemate *endo*-dithia[9]helicene-**2**: Monoclinic unit cell, space group $P2_1/n$, *a* = 9.712(2), *b* = 9.709(3), *c* = 25.072(6) (Å); α = 90, β = 94.401(7), γ = 90°; *Z* = 4; CCDC number 2184341. The experimental and calculated (CAM-B3LYP/def2-SV(P)) structures, reported in cyan and magenta respectively, are overlapped and shown below the unit cell. The root mean square deviation (RMSD, in Å) is calculated considering only the heavy atoms of an isolated dithia[9]-helicene of (*M*) configuration for both isomers. For the crystal cells, ORTEP diagrams are shown with thermal ellipsoids drawn at 50% probability. The data was acquired at room temperature.

Experimental photophysical and chiroptical properties and theoretical simulation of *exo*-dithia[9]helicene-1 and *endo*-dithia[9]helicene-2, and comparison with their [7]homologues

The UV-vis spectra of **1** and **2**, depicted in Fig. 2a, were measured in CH_2Cl_2 solution at concentrations *ca.* 10^{-5} M. *exo*-Dithia[9]helicene **1** displays (i) one intense band ($\varepsilon >$ 100 000 M^{-1} cm^{-1}) at 270 nm, accompanied with a slightly distinguishable band at higher energy ($\varepsilon \sim$ 58 000 M^{-1} cm^{-1} at 244 nm) and a shoulder at lower energy ($\varepsilon \sim$ 18 000 M^{-1} cm^{-1} at 320 nm), (ii) and one wide band ($\varepsilon \sim$ 16 000 M^{-1} cm^{-1}) centered at 360 nm. *endo*-Dithia[9]helicene **2** displays two intense bands at 250 and 285 nm ($\varepsilon \sim$ 60–70 000 M^{-1} cm^{-1}) and a wide band at 360 nm ($\varepsilon \sim$ 16 000 M^{-1} cm^{-1}). Overall the UV-vis response is similar for **1** and **2** in the low-energy region and differs in the high-energy with a red shift of the stronger band for compound **2** and the presence of an additional one. To shed some light on the electronic origin of these bands, time-dependent DFT (TD-DFT) calculations were performed (*vide infra*).

The electronic circular dichroism (ECD) spectra and optical rotation (OR) values of enantiopure samples of *exo*- and *endo*-dithia-[9]helicenes **1** and **2** were then measured (Fig. 2a, and Table 1). Both systems display strong specific rotation values ($[\alpha]_D^{25}$ = +5544 and +6940 for (*P*)-**1** and (*P*)-**2**, respectively in CH_2Cl_2 at concentrations of 10^{-5} M).[20] As depicted in Fig. 2a, the (*M*) and (*P*) enantiomers display the expected mirror-image ECD spectra. The different sets of bands observed in UV-vis spectra are strongly ECD active in both **1** and **2**. For instance,

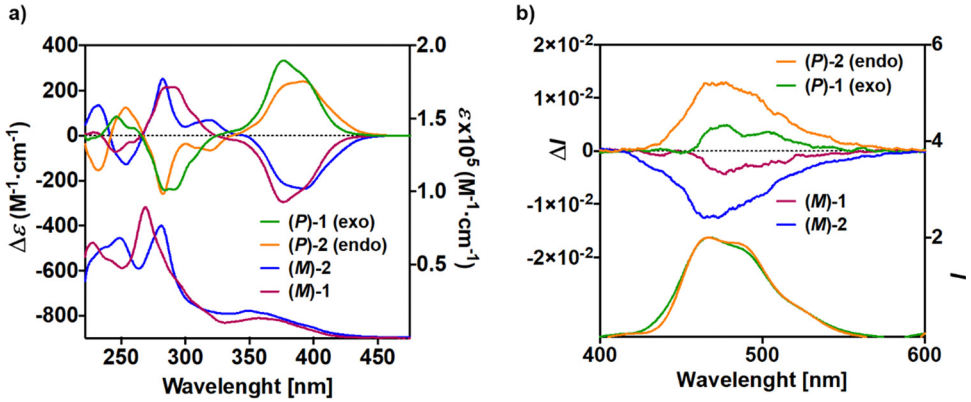

Fig. 2 (a) Experimental UV-vis (bottom) and ECD (top) spectra and (b) fluorescence (bottom) and CPL (top) spectra of (*P*) and (*M*) enantiomers of **1** and **2** (CH_2Cl_2, $C \sim 10^{-5}$ M).

Table 1 Specific optical rotations measured in CH_2Cl_2, at $C \sim 3\,8 \times 10^{-3}$ M; units are deg. g^{-1} mL dm^{-1}

$[\alpha]_D^{25}$	*exo*-Dithia[9]helicene (*P*)-**1**	*exo*-Dithia[9]helicene (*M*)-**1**	*endo*-Dithia[9]helicene (*P*)-**2**	*endo*-Dithia[9]helicene (*M*)-**2**
	+5544	−5310	+6940	−6772
$[\alpha]_D^{25}$	*exo*-Dithia[7]helicene (*P*)-**10**	*exo*-Dithia[7]helicene (*M*)-**10**	*endo*-Dithia[7]helicene (*P*)-**11**	*endo*-Dithia[7]helicene (*M*)-**11**
	+3342	−3377	+3548	−3595

exo compound (*P*)-**1** displays two moderate positive bands at 245 nm ($\Delta\varepsilon$ = +80 M^{-1} cm^{-1}) and 262 nm (+33), two strong negative bands at 284 (−241) and 291 (−240) and one shoulder at 306 (−103), and two strong positive bands 377 (+331) and 392 (+268) nm. Overall, the *endo* compound exhibits a similar ECD spectral envelope. Indeed, (*P*)-**2** displays (i) one positive band at 255 nm ($\Delta\varepsilon$ = +120 M^{-1} cm^{-1}), (ii) one strong negative band at 283 (−259), and two moderate ones at 309 (−54), and 319 (−65), and (iii) two strong positive bands at 378 (+227) and 395 nm (+236).

The UV-vis spectra of **10** and **11**, depicted in Fig. 3, were also measured in CH_2Cl_2 solution at concentrations *ca.* 10^{-5} M. *exo*-Dithia[7]helicene **10** displays two intense bands (ε > 30 000 M^{-1} cm^{-1}) at 240 and 267 nm, accompanied with one shoulder at 259, and a set of bands at 332, 354 and 396 nm together a very weak band at 419 nm. *endo*-Dithia[7]helicene **11** displays quite similar absorption spectrum, more specifically two intense bands (ε > 40 000 M^{-1} cm^{-1}) at 242 and 254 nm, accompanied with one distinguishable band at lower energy ($\varepsilon \sim$ 17 000 M^{-1} cm^{-1} at 290 nm), and a set of several bands of

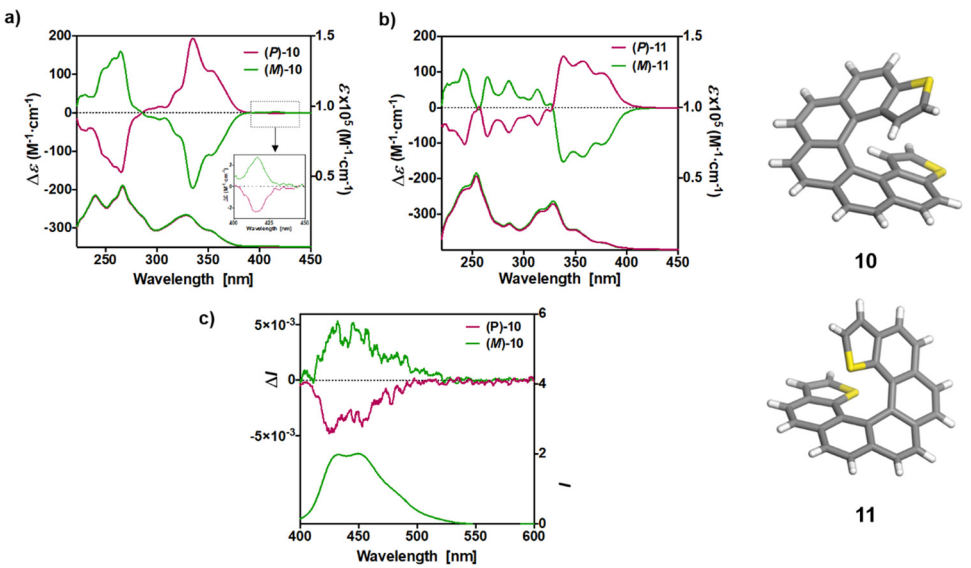

Fig. 3 The experimental UV-vis (bottom) and ECD (top) spectra of the (*P*) and (*M*) isomers of **10** and **11** (CH_2Cl_2, $C \sim 10^{-5}$ M) are shown in panels (a and b), respectively. The inset in (a) shows the magnified ECD of (*P*) and (*M*)-**10** in the 400–450 nm region. The fluorescence (bottom) and CPL (top) spectra of (*P*) and (*M*)-**10** are shown in panel (c).

moderate magnitude at 318, 330, 350, 379 nm together a very weak band at 426 nm.

The ECD spectra and OR values of enantiopure samples of *exo*- and *endo*-dithia-[7]helicenes **10** and **11** were also measured (Fig. 3 and Table 1). Both systems display strong specific rotation values ($[\alpha]_D^{25}$ = +3340 and +3550 for (*P*)-**10** and (*P*)-**11**, respectively) that are almost half those of dithia[9]helicenes **1** and **2**. The different sets of bands observed in UV-vis spectra are ECD active and the (*M*) and (*P*) enantiomers display the expected mirror-image ECD spectra. For instance, *exo* compound (*P*)-**10** displays a moderate negative band at 230 nm ($\Delta\varepsilon$ = −46 M^{-1} cm^{-1}), a structure of several intense negative bands at 250, 260 and 265 nm (−111, −141 and −154), a set of weak to moderate positive bands at 293, 303 and 319 nm (+10, +16 and +53), and two intense positive bands at 336 nm (+191), and 355 nm (+108). Finally, a very weak negative band (−2.4) is observed at 416 nm. Although weak, it is highly important because it dictates the sign of the CPL signal (*vide infra*). The *endo* compound (*P*)-**11** displays a set of four well-separated negative bands at 242, 265, 286 and 312 nm ($\Delta\varepsilon$ = −101, −79, −69, −48 M^{-1} cm^{-1}) together with some shoulders, and a set of three well-separated positive bands at 340, 360 and 378 nm (+140, +130, +92), together a slightly positive band at 420 nm (+1.4). Overall, the ECD spectrum of (*P*)-**11** is quite different, showing red-shifted and more defined signals than (*P*)-**10**.

The luminescence properties of compounds **1–2** and **10–11** were examined in CH_2Cl_2 at room temperature (r.t., 298 K). The r.t. emission of the *exo* derivative **1** is displayed in Fig. 2b, showing fluorescence signals at 466, 473 and 526 nm. The structuration most probably originated from the vibronic structures. Furthermore, a very low quantum yield of fluorescence (Φ_F = 0.2% at 470 nm) was measured. The *endo* derivative **2** displayed the same structured fluorescence signals at similar wavelengths and a higher quantum yield Φ_F of 3.5% at 470 nm. The [7]helicene derivatives **10** and **11** also exhibit extremely weak fluorescence signals. Interestingly, although weakly fluorescent, all compounds exhibit a signal at low temperature which is assigned to classical phosphorescence (see Fig. S2-1, ESI†). This is in line with a comparatively strong spin–orbit interaction which promotes intersystem crossing already observed in longer helicenes.[21]

Helicenes are known to exhibit efficient circularly polarized fluorescence or phosphorescence activity, which makes them appealing for incorporation into OLEDs as circularly polarized electroluminescent materials.[10] However, most thiahelicene derivatives do not emit light and few CPL-active systems have been reported.[13] The CPL spectra of the (*P*) and (*M*) enantiomers of **1** and **2** derivatives were recorded in CH_2Cl_2 at rt (Fig. 2b). Satisfyingly, the enantiomers revealed nice mirror-image CPL activity. Regarding the dissymmetry factors, which reflect the percentage of circularly polarized emitted light ($g_{lum} = 2(I_L - I_R)/(I_L + I_R)$), we obtained g_{lum} of -4.2×10^{-3}/$+4.6 \times 10^{-3}$ for **1** and -1.23×10^{-2}/$+1.25 \times 10^{-2}$ for **2**, for (*M*)/(*P*) enantiomers, respectively. Interestingly, the *endo* derivative displays a much higher absolute g_{lum} value than the *exo* derivative, with a 10^{-2} order of magnitude, among the highest in helicenes and other heteroaromatic helicene-like compounds.[11] These results nicely highlight the impact of the chemical structure and regioisomerism in heterohelicenes on the final photophysical and chiroptical properties since two *exo* and *endo* isomers display different CPL intensities. The fact that **2** displays higher g_{lum} values as compared to **1** is in agreement with theoretical calculations (*vide infra*). Note that for these measurements much care must be paid and very low concentrations must be used (around 10^{-5} M). Finally, due to very low emission signal, only *exo*-dithia[7]helicene **10** was found to display CPL activity ($\pm 5 \times 10^{-3}$) with low g_{lum} values and inverted signals (positive for (*M*) and negative for (*P*), Fig. 3b). Indeed, the CPL sign is in agreement with the ECD sign of low-energy band found at 415 nm (Fig. 3a inset and ESI†).

Theoretical analysis

The absorption and emission properties of both isomers of dithia[9]helicene, as well as of the smaller dithia[7]helicene, were investigated using Kohn–Sham density functional theory (KS-DFT) and its time-dependent (TD) extension. See ref. 23 and 24 regarding general strategies of modeling chiroptical parameters with TD-DFT and other electronic structure methods. The CAM-B3LYP functional[25] and the def2-SV(P) basis set[26] were employed for all calculations. Section S2 in the ESI† provides additional computational details. The spectra obtained with CAM-B3LYP are usually in satisfactory agreement with experiments, but overestimation of the transition energies up to about 0.5 eV for helicene systems has been noted in previous research.[27] For this work, a shift of −0.40 eV—optimal for the *exo*-dithia[9]helicene compound—was adopted for *endo*-dithia[9]helicene and the two dithia[7]helicenes as well, although it appears that a slightly smaller shift may already be sufficient. The calculations for *exo*-dithia[9]helicene and *endo*-dithia[7]helicene were performed with the (*P*) isomer, but for consistency the (*M*) isomer is considered in the following discussion. The signs of the chiroptical properties were inverted accordingly. Given the lack of experimental emission and CPL data for *endo*-dithia[7]helicene **11**, most of the theoretical analysis focuses on the dithia[9]helicenes **1** and **2**, and on *exo*-dithia[7]helicene **10**. The calculated absorption and ECD spectra of *endo*-dithia[7]helicene are briefly commented on.

Because of the C_2 symmetry of the compounds, the excited states have either ^{1}A or ^{1}B symmetry. Inspection of the TD-DFT spectra revealed that the transitions involving the states relevant for CPL—the ground state, S_0, and the first excited state, S_1—have ^{1}A symmetry. The dominant contributions to the transitions involve the HOMO−1, HOMO, LUMO, and LUMO+1 orbitals, shown in panel E of Fig. 5–7, that extend over the helicene core. The same orbitals are also involved in the S_0–S_1 transition for (*M*)-*endo*-dithia[7]helicene, see panel C of Fig. 8. The optimized geometries of the S_0 and S_1 states of (*M*)-*exo*-dithia[9]helicene **1** and (*M*)-*endo*-dithia[9]helicene **2** appear very similar, suggesting no substantial molecular rearrangement in the excited state. This is true for (*M*)-*exo*-dithia[7]helicene **10** as well. A comparison of the equilibrium geometries of both states for the three compounds is shown in Fig. S15 in the ESI.† For each of the four molecules, the calculated absorption and ECD

spectra (after energy-shifting) show good agreement with their experimental analogues (*vide infra*). For the CPL spectra, it was found that the simultaneous inclusion of Franck–Condon (FC) and Herzberg–Teller (HT) vibronic effects is necessary to obtain good agreement with the experimental data (panel D in Fig. 5–7). FC effects alone are not sufficient, as they result in spectra exhibiting a positive sign, like the purely electronic spectra but opposite to the experimental results. It is the combination with the negative intensities calculated including HT effects that yields calculated spectra matching the experimental band signs. See Section S2 in the ESI† for additional details on the spectra calculated with FC, HT, and FC + HT effects, and Fig. S16 (ESI†) for their visual comparison.

The purely electronic spectra of the two dithia[9]helicenes do not reproduce the experimentally observed negative CPL signs. Similar cases have been discussed previously.[28] In both cases, the calculated electronic rotatory strengths are found to be positive, a feature that is attributable to the angle, θ, between the transition electric and magnetic dipole moments being close to 0°, as shown in panels A and B of Fig. 4. The magnitude of the purely electronic rotatory strengths for the S_1–S_0 transitions is rather small (see Tables S1 and S2 in the ESI†), but in the case of (*M*)-*exo*-dithia[9]helicene this positive contribution to the vibrationally resolved spectrum can still be observed in the region around the 0–0 transition (panel D of Fig. 5), where it is not cancelled by HT effects. The spectrum obtained for the *endo* isomer does not exhibit any positive peaks, probably because the electronic contributions coming from the smaller rotatory strength of this compound are more effectively canceled by the FC + HT treatment. The calculated spectrum of *exo*-dithia[7]helicene exhibits a positive sign at the purely electronic level (panel C of Fig. 4). This compound has the largest rotatory strength among the four molecules (Table S3 in the ESI†). In contrast to the two dithia[9]helicenes, the intensity calculated at the FC level is greater than the intensity calculated at the HT level, resulting in the overall positive sign of the vibrationally resolved spectrum showed in panel D of Fig. 7.

The dissymmetry factors (g_{lum}) were calculated as $\Delta I/I$, *i.e.* as the ratio between the broadened calculated CPL (ΔI) and emission (I) intensities at the experimental wavelengths, instead of using the rotatory and dipole strengths of the electronic transitions, because of the aforementioned sign problem for the purely electronic transitions of the two dithia[9]helicenes.[29] The resulting g_{lum} for the two [9]helicenes are in reasonable agreement with the experiments, albeit overestimated for both compounds (Table 2). The calculated g_{lum} of (*M*)-*exo*-dithia[7]helicene is very close to the experiment (third row of Table 2).

The electronic absorption spectrum of (*M*)-*exo*-dithia[9]-helicene **1** (panel A of Fig. 5) exhibits an intense band around 270 nm accompanied by a less intense shoulder around 230 nm, closely resembling the experiment. Additional bands can be observed around 330 and 380 nm. For the ECD spectrum (panel B, Fig. 5), the most intense band is centered around 380 nm, and matches the experimental intensity in both sign and magnitude. The region between 270 and 350 nm appears more structured than the experiment, showing two major bands with positive sign while only one appears in the experimental spectrum. There is a good match between the calculated and experimental bands below 270 nm. The vibrationally resolved calculated emission spectrum (panel C, Fig. 5) is in good agreement with the experiment, but the latter shows less structure. The negative CPL intensity is mostly due to HT effects, although an incomplete cancellation between the FC and HT effects is responsible for the positive band calculated for the 0–0 transition for this compound. This is also observed from the purely electronic transition, as briefly mentioned above (see Section S2 in the ESI† for more details). Apart from this weak positive peak, the calculated CPL spectrum exhibits a major negative peak followed by three less intense bands, which match the structure of the experimental spectrum (panel D of Fig. 5). As mentioned before, the S_1–S_0 transition is assigned to transitions among HOMO−1, HOMO, LUMO, and LUMO+1, shown in panel E of Fig. 5. The orbitals appear delocalized over the helicene

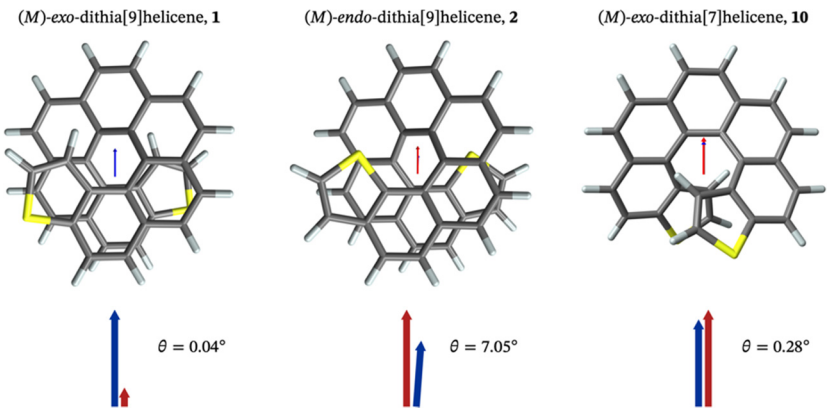

Fig. 4 Electric ($\vec{\mu}_e$, red arrows) and magnetic ($Im[\vec{\mu}_m^*]$, blue arrows) transition dipole moments—arbitrarily scaled relative to the images of the excited state (S_1) geometry—for the S_1–S_0 transition for the (*M*) isomers of *exo*-dithia[9]helicene (panel A), of *endo*-dithia[9]helicene (panel B), and of *exo*-dithia[7]helicene (panel C) obtained from TD-DFT calculations. For clarity, the electric and magnetic dipole moments are also shown, magnified, below the calculated geometries. The angle θ (in degrees) between the two vectors is shown as well. The transition moment vectors are collinear with the C_2 axes of the three compounds.

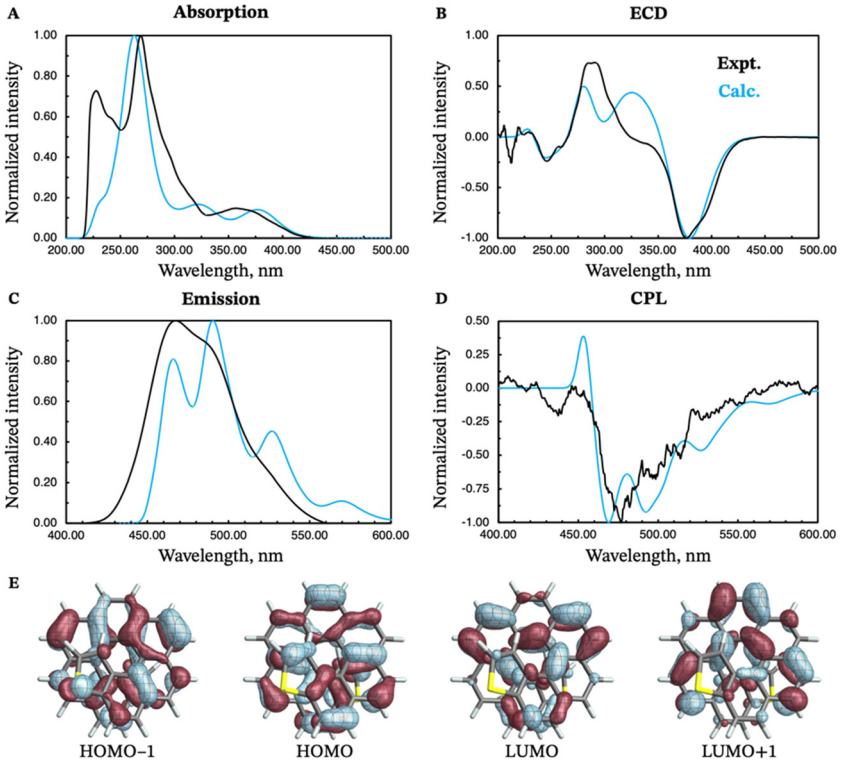

Fig. 5 Experimental (black curves) and calculated (blue curves) absorption (panel A), ECD (panel B), emission (panel C) and CPL (panel D) spectra of (*M*)-*exo*-dithia[9]helicene **1**. Isosurfaces (±0.03 au) for the most relevant frontier molecular orbitals (HOMO−1, HOMO, LUMO, and LUMO+1) are shown in panel E. The calculated energies were shifted by −0.40 eV prior to conversion to wavelengths.

Table 2 Experimental quantum yields and CPL activity of dithiahelicenes

Compound isomer	ϕ_F(%)	Solvent (conc., M)	CPL λ_{exp} (nm)	g_{lum}, expt	g_{lum}, calc
(*M*) *exo*-Dithia[9]helicene (**1**)	0.2	CH_2Cl_2 (10^{-6})	470	−0.0042	−0.019
(*M*) *endo*-Dithia[9]helicene (**2**)	3.5	CH_2Cl_2 (10^{-6})	470	−0.0125	−0.024
(*M*) *exo*-Dithia[7]helicene (**10**)	0.3	CH_2Cl_2 (10^{-6})	475	0.0050	0.0024
endo-Dithia[7]helicene (**11**)	0	CH_2Cl_2 (10^{-6})	—	—	
[9]Helicene[22]	0.014	1,4-Dioxan ($5{\cdot}10^{-4}$)	Unreported		
[7]Helicene[22]	0.021	1,4-Dioxan ($5{\cdot}10^{-4}$)	Unreported		

ϕ_F Fluorescence quantum yield (ratio emitted/absorbed photons). g_{lum} emission dissymmetry factor.

scaffold without contributions from the sulfur atom, except for HOMO−1.

Similar observations can be made for (*M*)-*endo*-dithia[9]-helicene **2**. The calculated absorption spectrum (panel A, Fig. 6) exhibits two bands in the region between 240 and 280 nm. The intensity of the band at higher wavelength is weaker than the one observed experimentally, although the positions match well, and the shoulder around 350 nm is matched by the calculations in both position and intensity. The ECD spectrum (panel B of Fig. 6) shows a major negative band centered around 380 nm. Other peaks at 340, 280 and 240 nm match the experimental spectral shape. The emission spectrum of the *endo* isomer is very similar to the emission spectrum of the *exo* isomer, and it shows the same bands. The vibrationally resolved CPL spectrum exhibits a relatively strong negative band corresponding to the 0–0 transition around 470 nm, followed by two additional shoulders (one at around 490 and the other at around 530 nm) that match the less-structured experimental spectrum closely. As for the *endo* compound, the S_1–S_0 transition is assigned to transitions among HOMO−1, HOMO, LUMO, and LUMO+1 (panel E in Fig. 6). These orbitals appear qualitatively similar to those of the *exo* isomer, as one would expect given the structural similarity of the two compounds. The orbitals are delocalized over the helicene scaffold. Some density on the sulfur atom is observed for the HOMO−1, like for the previous case.

The calculated and experimental spectra of (*M*)-*exo*-dithia[7]helicene **10** are compared in Fig. 7, panels A–D. The calculated absorption spectrum shows two major peaks, one around 260 nm, and the other around 330 nm. The most intense peak exhibits two almost symmetric shoulders (230 nm, 290 nm). The calculated ECD spectrum has an intense negative band around 340 nm, and a positive band around 250 nm, both matching the experiment in position and intensity. The calculated

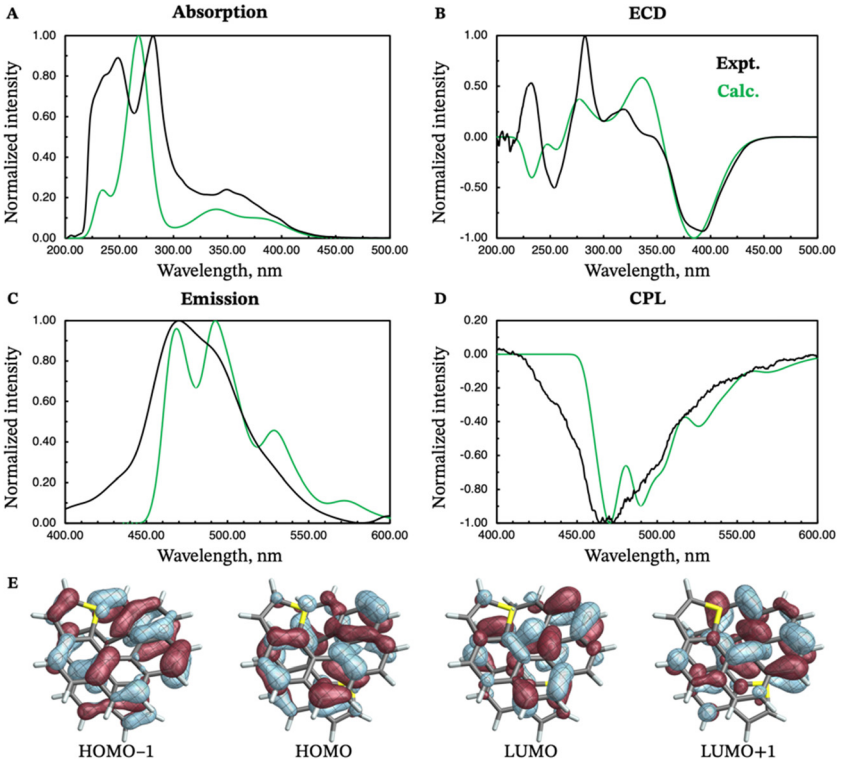

Fig. 6 Experimental (black curves) and calculated (green curves) absorption (panel A), ECD (panel B), emission (panel C) and CPL (panel D) spectra of (*M*)-*endo*-dithia[9]helicene **2**. Isosurfaces (±0.03 au) for the most relevant frontier molecular orbitals (HOMO−1, HOMO, LUMO, and LUMO+1) are shown in panel E. The calculated energies were shifted by −0.40 eV prior to conversion to wavelengths.

emission spectrum is similar in both shape and structure to the two [9]helicenes, except shifted towards shorter wavelengths. It also appears more structured than the experimental analogue, which only exhibits two major peaks centered around 450 and 430 nm. The calculated CPL spectrum, shown in panel D of Fig. 7, correctly reproduces the position of the two main bands at 430 and 450 nm. The calculated g_{lum} of this compound is smaller than any of the two [9]helicenes, in agreement with the experimental measurements. The compound also retains the electronic properties of the larger analogues, as mentioned earlier.

Due to the lack of experimental emission and CPL data for (*M*)-*endo*-dithia[7]helicene **11**, these spectra have not been calculated. Only the absorption and ECD spectra are compared to their experimental counterparts in Fig. 8. The absorption spectrum (panel A) is characterized by two major peaks centered near 310 and 240 nm. The most intense peak also shows a small shoulder around 200 nm. The calculated ECD spectrum is characterized, similarly to the *exo* isomer, by an intense negative band around 340 nm, followed by a positive band of similar intensity around 300 nm (panel B of Fig. 8). Both bands match the experimental position and intensity, although the experimental spectrum appears more structured across the whole experimental window. The HOMO−1, HOMO, LUMO, and LUMO+1 orbitals (panel C) are all involved in the S_0–S_1 transition. They appear delocalized over the whole molecule, and they are—perhaps unsurprisingly—qualitatively similar to those of the *exo* isomer. Only the HOMO−1 orbital is significantly delocalized over the sulfur atoms, similarly to the other isomer and the dithia[9]helicenes.

Characterization on a gold surface of *exo*- and *endo*-dithia[9]helicenes 1 and 2. Unveiling the chirality of a single molecule by STM topography at room temperature

Scanning Tunneling Microscopy (STM) is one of the most successful techniques available that can be used for identifying the chirality of both enantiomers at ambient conditions. In line with our former studies looking for nanoscaled solenoids,[13] we characterized our *exo*- and *endo*-dithia[9]helicenes on a gold electrode.[15] Prior to the topography study, the (111) crystallographic orientation of a gold substrate is prepared through a flame-annealing process. The deposition of the molecules was performed using drop casting followed by a dried step with argon gas and vacuum up to 10^{-2} mbar. During this study, we worked using a solution in benzene in a concentration of 0.3 mg mL^{-1}. Topographic images were acquired using a $Pt_{90}Ir_{10}$ tip and a bias voltage around 0.5 V to the sample in a constant current mode. The current amplification is 10^9 V A^{-1}. Thanks to the flatness of the surface, it is possible to visualize the molecular distribution and distinguish single molecules. It should be pointed out that reports of single helicene molecules imagining are confined only to low temperature and ultra-high vacuum conditions.[30]

Panel (a) of Fig. 9 shows a STM image of the *exo*- topology decorating the (111) gold terraces. In general, no ordering along

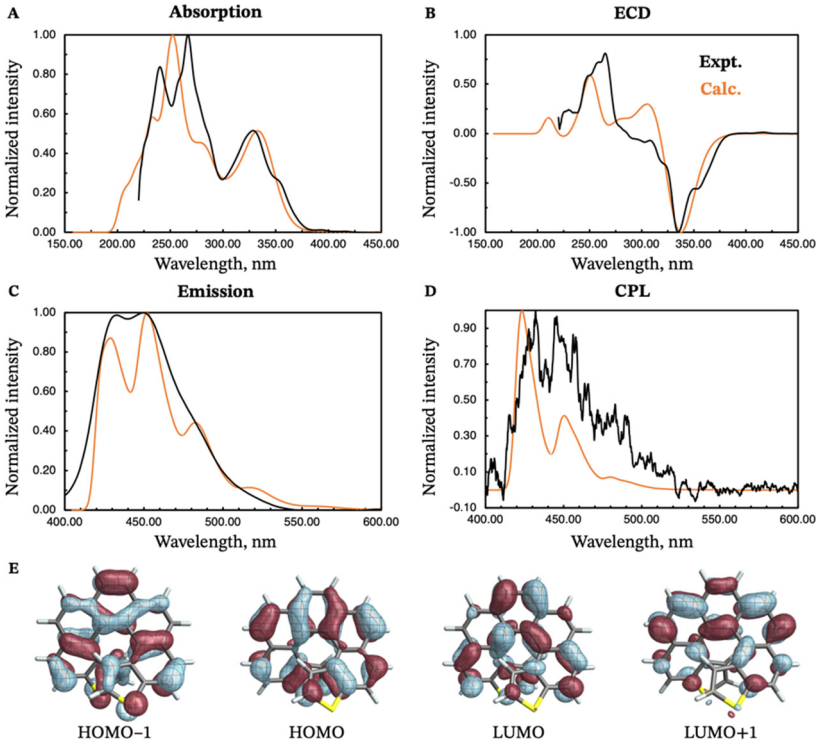

Fig. 7 Experimental (black curves) and calculated (orange curves) absorption (panel A), ECD (panel B), emission (panel C) and CPL (panel D) spectra of (*M*)-*exo*-dithia[7]helicene **10**. Isosurfaces (±0.03 au) for the most relevant frontier molecular orbitals (HOMO−1, HOMO, LUMO, and LUMO+1) are shown in panel E. The calculated energies were shifted by −0.40 eV prior to conversion to wavelengths.

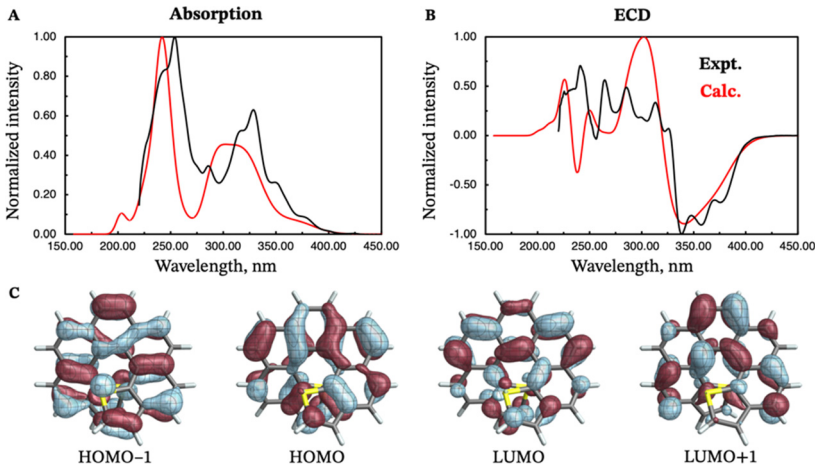

Fig. 8 Experimental (black curves) and calculated (red curves) absorption (panel A) and ECD (panel B) spectra of (*M*)-*endo*-dithia[7]helicene **11**. Isosurfaces (±0.03 au) for the most relevant frontier molecular orbitals (HOMO−1, HOMO, LUMO, and LUMO+1) are shown in panel C. The calculated energies were shifted by −0.40 eV prior to conversion to wavelengths.

the (111) gold terraces is found, although mono or bilayers of molecules without an apparent ordered pattern could be detected. Panel (b) presents an STM image where the two enantiomeric are identified. Green and blue colored circles reveal the mirror-image forms of dithia[9]helicenes, labeled as B1 and B2. For identifying the handedness, panels (B1) and (B2) provide the height profiles *versus* the distance of the selected molecules following the arrow across the diagonal. Inset illustrations show how the measured molecules are oriented. As criteria, we start from the arrow's nock, positioned close to the highest part of the molecule, up to the head. Together with the measured topography of the scanning, we can clearly identify first, that the molecules present unevenness related to the helix structure, which is an indication that we are measuring the target molecules. Considering the evolution of the recorded intensity along the helix, we can clearly identify

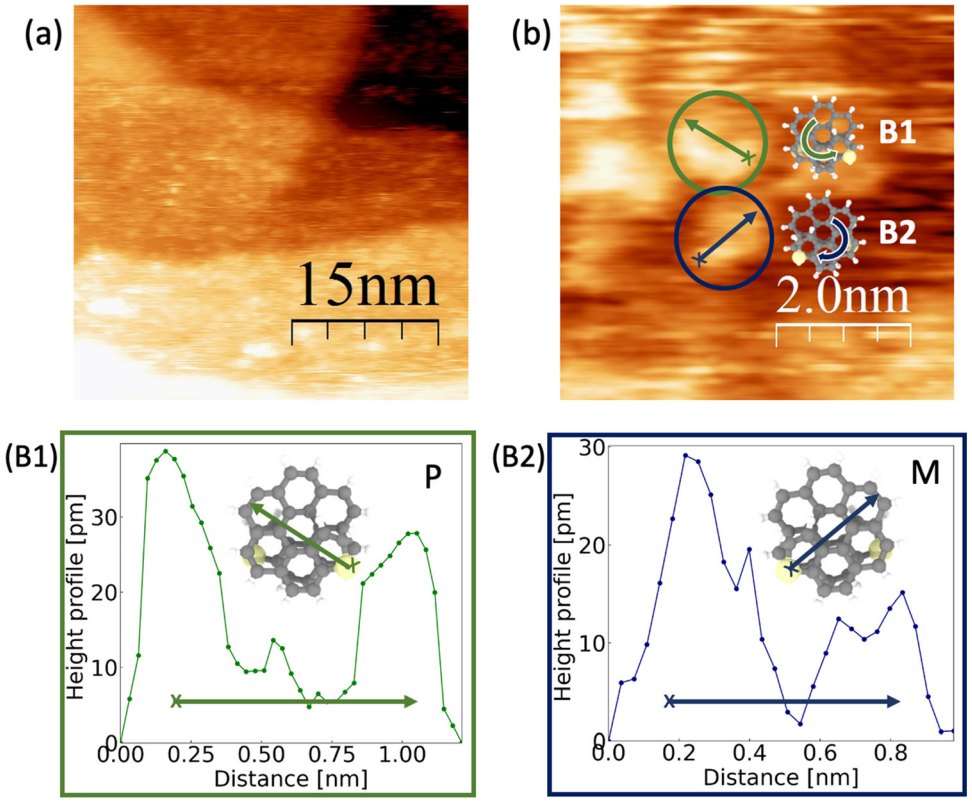

Fig. 9 Panel (a) shows a topographic image of *exo*-dithia[9]helicene acquired using V_{bias} = 0.5 V and I_t = 0.1 × 10^{-9} A. (b) Zoomed in image of two enantiomer with chirality *P* in green and *M*, in blue, and the corresponding height profiles for each enantiomer (B1 for *P* and B2 for *M*). The set parameters were V_{bias} = 0.4 V and I_t = 0.1 × 10^{-9} A.

the observed chiralities, *i.e. P* in green and *M* in blue. Moreover, the direction of the helix of the molecules can be related to the schematic models following the arrow along the structure (see the schematic model in panel (b)). This was also the case for the smaller homologue *exo*-dithia[7]helicene, which suggests the role of the sulfur atom as an anchoring site of the molecule. Further topographic images of the resolved enantiomers can be found in the ESI.†

Conclusions:

We have implemented a LED-driven methodology to carry out a straightforward synthesis of *exo*- and *endo*-dithia[9]helicenes **1** and **2** using a double photocyclization key step that leads to the desired helicene regiochemistry in good yields. *P* and *M* enantiomers of both *exo*- and *endo*-dithia[9]helicene products were isolated and fully characterized, by X-ray crystallography, in solution, *in silico* and by STM. The symmetric positioning of the sulfur atoms as anchoring groups in the molecule precludes a scenario of multiple orientations on the gold surface, making it possible to identify the chirality of the isolated molecules *via* STM topography at room temperature. *endo*-Dithia[9]helicene-**2** displays an experimental dissymmetry factor (g_{lum} = 1.2·10^{-2}) about three times larger than its isomer, *exo*-dithia[9]helicene, and of its smaller homologue *endo*-dithia[7]helicene. The theoretical calculations reproduce this behavior, although semi-quantitative agreement with the experiment is achieved, and highlight the impact of (1) magnetic and electronic dipole transition moments, (2) HT and FC contributions, on the overall chiroptical responses.

It is still early to determine whether this is an isolated event, but a one-order magnitude of amplification of the dissymmetry factor has been also reported in an extended [7]helicene (g_{lum} = 0.77·10^{-3}) compared to its longer [9]helicene homologue (g_{lum} = 7.44·10^{-3}).[31] This opens the gate for further studies trying to relate the structural-CPL response relationships on a larger sampling of structurally related systems in order to determine the underlying factors behind this enhanced dissymmetry factor.

Author contributions

This work is the result of the cooperation between three main research teams from the University of Alicante, the University of Rennes and the State University of New York. B. C. B., P. J. B. and A. G. carried out the synthesis, spectroscopic and crystallographic characterization of the thiahelicenes considered in this work. T. d. A., C. S. and C. U. did the STM characterization as single molecules adsorbed on gold. R. R., N. V. and J. C. performed the separation of enantiomers and determined their photophysical and chiroptical properties. P. M. and J. A. carried

out the theoretical studies of the chiroptical properties of these compounds.

Conflicts of interest

There are no conflicts to declare.

Acknowledgements

A. G. and C. U. thank the financial support by the Spanish MICIIN (PID2019-109539GB-C41), the Generalitat Valenciana (PROMETEO/2021/017), and the University of Alicante (VIGROB-285). C. S. thanks for the financial support by the Generalitat Valenciana through CDEIGENT2018/028. The computational resources provided by the Department of Applied Physics of the University of Alicante are greatly appreciated. J. A. and P. M. thank the National Science Foundation, grant CHE-1855470, for support of the theoretical component of this study, and the Center for Computational Research (CCR) at the University at Buffalo for providing computational resources. J. C. thanks the Ministère de l'Education Nationale, de la Recherche et de la Technologie and the Centre National de la Recherche Scientifique (CNRS). R. R. Thanks Xunta de Galicia for a Postdoctoral Fellowship.

References

1 C.-F. Chen and Y. Shen, Helicene Chemistry, *From Synthesis to Applications*, Springer-Verlag: Berlin, Heidelberg, Germany, 2017, pp. 231–245.
2 M. Gingras, *Chem. Soc. Rev.*, 2013, **42**, 1051–1095.
3 J. P. Riehl and G. Muller, *In Comprehensive Chiroptical Spectroscopy: Instrumentation, Methodologies, and Theoretical Simulations*, John Wiley & Sons, Inc., 2012, Volume 1, pp. 65–90.
4 (*a*) T. Mori, *Circularly Polarized Luminescence of Isolated Small Organic Molecules*, Springer, 2020; (*b*) L. E. MacKenzie, L.-O. Palsson, D. Parker, A. Beeby and R. Pal, *Nat. Commun.*, 2020, **11**, 1676.
5 T. Mori, *Chem. Rev.*, 2021, **121**, 2373–2412.
6 H. Tanaka, M. Ikenosako, Y. Kato, M. Fujiki, Y. Inoue and T. Mori, *Commun. Chem.*, 2018, **1**, 38.
7 See for instance: H. Kubo, T. Hirose, T. Nakashima, T. Kawai, J. Hasegawa and K. Matsuda, *J. Phys. Chem. Lett.*, 2021, **12**, 686–695.
8 K. Dhbaibi, L. Favereau and J. Crassous, *Chem. Rev.*, 2019, **119**, 8846–8953.
9 (*a*) Y. Sawada, S. Furumi, A. Takai, M. Takeuchi, K. Noguchi and K. Tanaka, *J. Am. Chem. Soc.*, 2012, **134**, 4080–4083; (*b*) K. Nakamura, S. Furumi, M. Takeuchi, T. Shibuya and K. Tanaka, *J. Am. Chem. Soc.*, 2014, **136**, 5555–5558; (*c*) K. Goto, R. Yamaguchi, S. Hiroto, H. Ueno, T. Kawai and H. Shinokubo, *Angew. Chem., Int. Ed.*, 2012, **51**, 10333–10336; (*d*) H. Oyama, K. Nakano, T. Harada, R. Kuroda, M. Naito, K. Nobusawa and K. Nozaki, *Org. Lett.*, 2013, **15**, 2104–2107; (*e*) M. Shyam Sundar, H. R. Talele, H. M. Mande, A. V. Bedekar, R. C. Tovar and G. Muller, *Tetrahedron Lett.*, 2014, **55**, 1760–1764; (*f*) T. Otani, A. Tsuyuki, T. Iwachi, S. Someya, K. Tateno, H. Kawai, T. Saito, K. S. Kanyiva and T. Shibata, *Angew. Chem., Int. Ed.*, 2017, **56**, 3906–3910; (*g*) C. Shen, M. Srebro-Hooper, M. Jean, N. Vanthuyne, L. Toupet, J. A. G. Williams, A. R. Torres, A. J. Riives, G. Muller, J. Autschbach and J. Crassous, *Chem. – Eur. J.*, 2017, **23**, 407–418; (*h*) R. Yamano, J. Hara, K. Murayama, H. Sugiyama, K. Teraoka, H. Uekusa, S. Kawauchi, Y. Shibata and K. Tanaka, *Org. Lett.*, 2017, **19**, 42–45.
10 (*a*) W. L. Zhao, M. Li, H.-Y. Lu and C.-F. Chen, *Chem. Commun.*, 2019, **55**, 13793–13803; (*b*) J. Crassous, *Circularly polarized luminescence in helicene and helicenoid derivatives in "Circularly Polarized Luminescence of Isolated Small Organic Molecules"*, T. Mori, ed., Springer, 2020, pp. 53–97.
11 E. M. Sánchez-Carnerero, A. R. Agarrabeitia, F. Moreno, B. L. Maroto, G. Muller, M. J. Ortiz and S. de la Moya, *Chem. – Eur. J.*, 2015, **21**, 13488–13500.
12 E. Licandro, S. Cauteruccio and D. Dova, Chapter One, *Adv. Heterocycl. Chem.*, 2016, **118**, 1–46.
13 Examples of sulfur-containing [9]helicenes:(*a*) Y. Yamamoto, H. Sakai, J. Yuasa, Y. Araki, T. Wada, T. Sakanoue, T. Takenobu, T. Kawai and T. Hasobe, *J. Phys. Chem. C*, 2016, **120**, 7421–7427; (*b*) Y. Yamamoto, H. Sakai, J. Yuasa, Y. Araki, T. Wada, T. Sakanoue, T. Takenobu, T. Kawai and T. Hasobe, *Chem. – Eur. J.*, 2016, **22**, 4263–4273; (*c*) F. Chen, T. Tanaka, Y. S. Hong, T. Mori, D. Kim and A. Osuka, *Angew. Chem., Int. Ed.*, 2017, **56**, 14688–14693; (*d*) J. Larsen and K. Bechgaard, *Acta Chem. Scand.*, 1996, **50**, 71–76; (*e*) Q. Zhang, Y.-F. Wu, S.-W. Ying, S.-D. Liao, L. Zhang, J.-J. Du, B.-W. Chen, H.-R. Tian, F.-F. Xie, H. Xu, S.-L. Deng, S.-Y. Xie and L.-S. Zheng, *Angew. Chem., Int. Ed.*, 2022, e202204334.
14 B. C. Baciu, T. de Ara, C. Sabater, C. Untiedt and A. Guijarro, *Nanoscale Adv.*, 2020, **2**, 1921–1926.
15 B. C. Baciu, J. A. Vergés and A. Guijarro, *J. Org. Chem.*, 2021, **86**, 5668–5678.
16 K. B. Jørgensen, *Molecules*, 2010, **15**, 4334–4358.
17 Root mean squared deviation calculated with Pymol: L. Schrödinger and W. DeLano (2020). PyMOL. Retrieved from **https://www.pymol.org/pymol**.
18 (*a*) P. Morgante and R. Peverati, *Chem. Phys. Lett.*, 2021, **765**, 138281; (*b*) R. Peverati and D. G. Truhlar, *Philos. Trans. R. Soc., A*, 2014, 20120476.
19 Y. Nakai, T. Mori and Y. Inoue, *J. Phys. Chem. A*, 2012, **116**, 7372–7385.
20 K. Dhbaibi, L. Favereau and J. Crassous, *Chem. Rev.*, 2019, **119**, 8846–8953.
21 M. Sapir and E. Vander Donckt, *Chem. Phys. Lett.*, 1975, **36**, 108–110.
22 E. Vander Donckt, J. Nasielski, J. R. Greenleaf and J. B. Birks, *Chem. Phys. Lett.*, 1968, **2**, 409–410.
23 M. Srebro-Hooper and J. Autschbach, *Annu. Rev. Phys. Chem.*, 2017, **68**, 399–420.

24 J. Autschbach, L. Nitsch-Velasquez and M. Rudolph, *Top. Curr. Chem.*, 2011, **298**, 1–98.
25 T. Yanai, D. P. Tew and N. C. Handy, *Chem. Phys. Lett.*, 2004, **393**, 51–57.
26 F. Weigend and R. Ahlrichs, *Phys. Chem. Chem. Phys.*, 2005, **7**, 3295–3305.
27 K. Dhbaibi, L. Abella, S. Meunier-Della-Gatta, T. Roisnel, M. Vanthuyne, B. Jamoussi, G. Pieters, B. Racine, E. Quesnel, J. Autschbach, J. Crassous and L. Favereau, *Chem. Sci.*, 2021, **12**, 5522–5533.
28 G. Longhi, E. Castiglioni, C. Villani, R. Sabia, S. Menichetti, C. Viglianisi, F. Devlin and S. Abbate, *J. Photochem. Photobiol., A*, 2016, **331**, 138–145.
29 Y. Liu, J. Cerezo, G. Mazzeo, N. Lin, X. Zhao, G. Longhi, S. Abbate and F. Santoro, *J. Chem. Theory Comput.*, 2016, **12**, 2799–2819.
30 K.-H. Ernst, *Acc. Chem. Res.*, 2016, **49**, 1182–1190.
31 Z. Qiu, C.-W. Ju, L. Frédéric, Y. Hu, D. Schollmeyer, G. Pieters, K. Müllen and A. Narita, *J. Am. Chem. Soc.*, 2021, **143**, 4661–4667.

